Optimized optical tomography of quantum states of a room-temperature alkali-metal vapor

Marek Kopciuch [1,2,*] Magdalena Smolis,[1] Adam Miranowicz [3] and Szymon Pustelny [1,†]

[1]*Institute of Physics, Jagiellonian University in Kraków, Łojasiewicza 11, 30-348 Kraków, Poland*

[2]*Doctoral School of Exact and Natural Sciences, Faculty of Physics, Astronomy and Applied Computer Sciences, Jagiellonian University, Łojasiewicza 11, 30-348 Kraków, Poland*

[3]*Institute of Spintronics and Quantum Information, Faculty of Physics, Adam Mickiewicz University, 61-614 Poznań, Poland*

(Received 4 September 2023; revised 23 January 2024; accepted 1 February 2024; published 1 March 2024)

We demonstrate an experimental technique for the quantum-state tomography of the collective qutrit states of a room-temperature alkali-metal vapor. It is based on the measurements of the polarization of light traversing the vapor subjected to a magnetic field. To assess the technique's robustness against errors, experimental investigations are supported with numerical simulations. This not only allows us to determine the fidelity of the reconstructed states, but also to analyze the quality of the reconstruction for specific experimental parameters, such as light tuning and the number of measurements. By utilizing the conditional number, we demonstrate that the reconstruction robustness can be optimized by a proper adjustment of experimental parameters, and further improvement is possible with the repetition of specific measurements. Our results demonstrate the potential of this high-fidelity reconstruction method of quantum states of room-temperature atomic vapors.

DOI: 10.1103/PhysRevA.109.032402

I. INTRODUCTION

Quantum technologies are founded upon the precise manipulation and reconstruction of quantum states. When dealing with single microscopic quantum objects, the reconstruction of states becomes challenging. This stems from a (usually) destructive nature of the reconstruction and small amplitudes of recorded signals. To address these difficulties, some researchers have turned their focus towards studying ensembles of quantum objects, which display a collective quantum behavior [1–15].

Atomic vapors serve as a prime example of a medium utilized for the engineering of collective quantum states. In their ultracold form, they allow for precise quantum control through light and other external fields, albeit the implementation of such control requires complex experimental setups. On the other hand, room-temperature vapors can be studied using simpler apparatuses, but they simultaneously present challenges in terms of theoretical understanding of to which extent collective ensembles are quantum [3]. Despite these problems, however, room-temperature atomic vapors were used to demonstrate various quantum-mechanical effects including coherent population trapping [4], spin squeezing [5,6], macroscopic entanglement [7,8], spin waves [8,9], squeezed-light generation [5,10,11], and the entanglement of light modes [12]. A rubidium vapor was also used to construct an on-demand quantum memory [13,14]. These experiments have revived the interest in such media, while also necessitating the development of reliable quantum state tomography (QST) methods.

In this work, we demonstrate an experimental implementation of the recently proposed QST method [15]. The method enables the reconstruction of a complete collective density matrix of a room-temperature atomic vapor. It is based on the illumination of the vapor with an off-resonant probing light, and monitoring properties of the light after traversing a medium subjected to an external magnetic field. This enabled us to reconstruct a collective quantum state of ^{87}Rb atoms residing in the $F = 1$ ground state (qutrit), as shown in Fig. 1.

To evaluate the efficiency of the tomographic technique, we used the so-called conditional number [16–18]. Previously, the parameter was used for a comprehensive comparison of the optical tomographic methods of two polarization qubits [17] or the nuclear magnetic resonance (NMR) tomography of two ^{1}H spins 1/2 (two qubits) [19] and a single nuclear spin 3/2 (a quartit) in a semiconductor quantum well [20]. We demonstrate that, by an appropriate tuning of a probing light, the conditional number can be minimized (corresponding to an optimized reconstruction), reaching as small value as 2.25. We also discuss the methods for further improvement of the reconstruction efficiency by repeating specific measurements.

II. PRINCIPLES OF THE OPTICAL TOMOGRAPHY

We begin with a brief overview of the QST technique developed in Ref. [15]. This method relies on measuring the polarization rotation of linearly polarized probe light traversing a medium (e.g., room-temperature alkali-metal atoms) subjected to a longitudinal magnetic field. We assume that the

*marek.kopciuch@doctoral.uj.edu.pl
†pustelny@uj.edu.pl

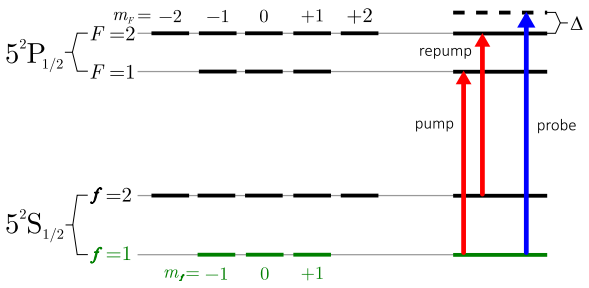

FIG. 1. Energy-level diagram corresponding to the ^{87}Rb D_1 line (presented energy gaps are not in scale), with measured qutrit marked with green. Additionally, tunings of all the laser beams are presented; red lines correspond to the pumping and repumping light used for the state preparation, and the blue line shows the probing beam which is blue detuned from the resonance by Δ and used for state reconstruction.

amplitude of the light is small, which allows us to describe its interaction with atoms using a perturbation theory of the lowest order (linear interaction). At the same time, unlike previous approaches (see, e.g., Refs. [21,22]), we do not assume a significant detuning of the light from the optical transition. This allows us to consider not only vector contributions to a polarization rotation [21,23,24], but also a tensor contribution [25], and hence reconstruct the whole collective density matrix of the atoms. It is noteworthy that this reconstruction is achieved without full control over the system, as successive magnetic sublevels are equally split due to a weak magnetic field (due to the linear Zeeman effect) and, hence, cannot be selectively addressed [26].

In Ref. [15], the relation between a time-dependent polarization rotation $\delta\alpha(t)$ and operators $\hat{\alpha}_{R,I}$ and $\hat{\beta}$ was introduced. These operators are associated with the coherence and population difference of specific magnetic sublevels and, hence, provide the access to specific density-matrix elements. In this work, we employ a slightly modified version of that relationship, i.e.,

$$\delta\alpha(t;\Delta) = \eta(\Delta)(e^{-\gamma_1 t}[\langle\hat{\alpha}_R\rangle \sin(2\Omega_L t) + \langle\hat{\alpha}_I\rangle \cos(2\Omega_L t)] - \zeta(\Delta)e^{-\gamma_2 t}\langle\hat{\beta}\rangle), \quad (1)$$

where $\eta(\Delta) = \chi V_R(\Delta)$ and $\zeta(\Delta) = V_I(\Delta)/V_R(\Delta)$ are the global and local scaling factors associated with the real (V_R) and imaginary (V_I) parts of the Voigt profile, respectively, and χ is related to experimental parameters, such as an atomic density and a transition frequency (for more details see Appendix A). As shown in Eq. (1), the time dependence of the polarization rotation is determined by the Larmor frequency Ω_L and the longitudinal and transverse relaxation rates γ_1 and γ_2.

Since a single measurement described by Eq. (1) allows us to extract only limited information about the system (specifically the population difference and the coherence between magnetic sublevels with $\Delta m_F = 2$), it is necessary to expand the set of measured signals to obtain a more comprehensive information. To achieve this, we introduce a series of unitary operations known as control pulses, which modify the state. This provides us the access to other density-matrix elements and, hence, offers a complete characterization of the system [15]. In turn, the reconstruction problem can be presented as [15]

$$\mathbb{O}\rho_V = \mathbf{b}, \quad (2)$$

where $\mathbb{O}$ represents the coefficient matrix determined by the set of observables, and $\rho_V = [\rho^R_{\bar{1}\bar{1}}, \rho^R_{\bar{1}0}, \rho^I_{\bar{1}0}, \ldots]^T$ (where $\rho^R_{mn} = \mathrm{Re}\{\rho_{mn}\}$ and $\rho^I_{mn} = \mathrm{Im}\{\rho_{mn}\}$, and $\bar{1} = -1$) is the vectorized form of a standard-form (square) density matrix ρ with elements ρ_{ij} (see Appendix A for more information). Moreover, $\mathbf{b}$ is the observation vector, which contains the values of measured observables. In a typical experimental scenario, the set of measurements, given in Eq. (2), is often overdetermined, and it is advantageous to rescale it to a more suitable form,

$$\mathbb{C}\rho_V = \tilde{\mathbf{b}}, \quad (3)$$

where $\mathbb{C} = \mathbb{O}^\dagger\mathbb{O}$ and $\tilde{\mathbf{b}} = \mathbb{O}^\dagger\mathbf{b}$. This rescaling enables the calculation of the density operator by simply inverting the aforementioned linear problem.

III. EXPERIMENTAL DETAILS

A. Experimental setup

The heart of our experimental system is a paraffin-coated spherical cell 3 cm in diameter, containing an isotopically enriched sample of ^{87}Rb atoms. The cell is heated up to 50 °C and placed inside a cylindrical magnetic shield made of three layers of mumetal and a qubic innermost ferrite layer (a shielding factor of about 10^5). Apart from the cell, the shield additionally contains a set of magnetic-field coils, which enables the residual-field compensation and generation of magnetic-field pulses in the **x**, **y**, and **z** directions. During the application of magnetic-field pulses, which rotate the states, other magnetic fields and all light beams are switched off. Light used for the illumination of the rubidium atoms is provided by three diode lasers, where the pump and probe lasers are distributed-feedback lasers (DFBs), and the repump laser is a Fabry-Pérot laser (ECDL). All the lasers are independently tuned, and the repump laser wavelength is frequency-stabilized using a dichroic atomic vapor laser lock (DAVLL) [27]. The wavelengths of the other two lasers are passively maintained due to their inherent temporal stability. Performance of all the lasers is monitored using a wave meter, while the pump and probe lasers are additionally monitored through saturated absorption spectroscopy (SAS). The intensities of the laser beams are dynamically controlled by three acousto-optical modulators (AOMs). To generate a specific quantum state in the vapor, the pump-light polarization is set by polarizers (POLs) and a quarter-wave plate (λ/4), while the repump light is linearly polarized in a direction orthogonal to the pump-light propagation direction (i.e., along the **y** axis). The **y** polarization of the probe light is provided by a Glan-Thomson polarizer placed before the shield and its polarization rotation after the medium is measured using a balanced polarimater consisting of a Wollastron prism (WOL) and a balanced photodetector (BPD). To determine the local scaling factor (see the discussion below), the intensity of the probe light is monitored prior to the shield. The schematic of the setup is shown in Fig. 2(a).

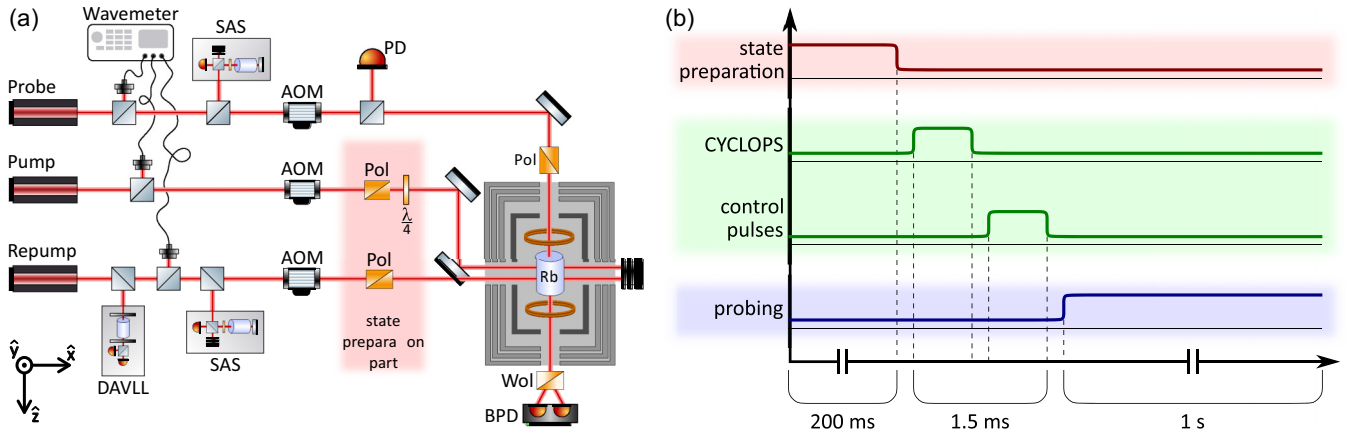

FIG. 2. (a) Simplified scheme of the experimental setup used for the quantum-state generation and tomography of collective states of an alkali-metal vapor. SAS: Saturation absorption spectroscopy; DAVLL: Dichroic atomic vapor laser lock; AOM: Acousto-optic modulator; PD: Photodiode; Pol: Glan-Thompson polarizer; $\lambda/4$: Quater-wave plate; Rb: Parafin-coated vapor cell filled with ^{87}Rb; Wol: Wollaston prism; BPD: Balanced photodetector. (b) Experimental sequence used in our method. The initial state of atoms is prepared with the pump light turned on for about 200 ms (red trace). After the preparation period, we apply a sequence of magnetic pulses to modify the state of the atoms (green trace). Here, the CYCLOPS pulses (see Sec. III D) are first used and then the control pulses are implemented for a total time of about 1.5 ms. Finally, the probe light is turned on, alongside with the longitudinal magnetic field, for about 1 s (blue) and the polarization rotation signal is recorded.

B. Experimental sequence

The experimental sequence utilized in our measurements is shown in Fig. 2(b). The sequence begins with a pumping period during which a specific quantum state is engineered. This stage typically consists of a 200-ms light pulse (optical pumping), which is applied simultaneously with the repumping that prevents the atoms from escaping into the dark ($F = 2$) state, followed by a few short pulses ($\approx$100 μs, a rotation-angle uncertainty of 0.12°), enabling the generation of a desired complex state. Subsequently, a series of magnetic-field pulses is used to mitigate technical problems (see Sec. III D), which is followed by a set of control pulses. Once the pulses are completed, a constant magnetic field is applied along the **z** direction, ranging between 10 and 100 nT. At the same time, the probe light, propagating along **z** with an intensity of 1–20 $\mu W/cm^2$, is switched on. In order to improve the signal-to-noise ratio (SNR), the intensity of the probe light is modulated at a frequency of 200 kHz and a polarimeter signal is detected using a lock-in amplifier.

C. Global and local scaling factors

An important element of the reconstruction of the density matrix is the determination of the global scaling factor $\eta(\Delta)$ in Eq. (1). This can be done by measuring the light absorption in an unpolarized vapor. Using the absorption relationship derived in Appendix C, the factor can be identified by comparing the absorption of the probe light, tuned to the same wavelength as that during the tomography measurements (i.e., blue detuned from $f = 1 \to F = 2$ by 50–400 MHz), with the absorption of a far-detuned light (>15 GHz). The global scaling factor is given by

$$\eta(\Delta) = \frac{27}{16}\left(\sqrt{\frac{U_2(\Delta)/U_1(\Delta)}{U_2(\infty)/U_1(\infty)}} - 1\right), \tag{4}$$

where U_1 is the voltage measured at the transimpedance photodetector placed in front of the medium and U_2 after it [see Fig. 2(a) and Appendix C 1] with Δ indicating the probe light tuned for QST and ∞ stands for the far-detuned light.

Experimental determination of the local scaling factor, $\zeta(\Delta)$ in Eq. (1) presents a greater challenge. It requires the preparation of an anisotropic well-defined quantum state. In this work, we select "stretched" states along the **x** and **z** axes. This means that the state has maximal projection of its angular momentum on the respective axis. The first state can be created by illuminating the atoms with a circularly polarized pump light propagating along the **x** axis. The preparation of the second state is more involved and requires the application of an additional magnetic-field pulse after the optical pumping, which rotates the atomic **x** polarization to the **z** direction. Note that we have experimentally verified that this process did not introduce dephasing, as evidenced by the unchanged signal amplitude for a many-π pulse. Employing this procedure allows us to mitigate the systematic errors arising from varying polarization levels achieved with the pump light propagating along different directions, while simultaneously simplifying the experimental setup. The formulas for the light polarization rotation corresponding to these two states are (see Appendix C 2 for more details)

$$\delta\alpha^{(z)}(t;\Delta) = -\frac{5(1-\epsilon)}{24}\eta(\Delta)\zeta(\Delta)e^{-\gamma_2 t}, \tag{5}$$

$$\delta\alpha^{(x)}(t;\Delta) = -\frac{(1-\epsilon)}{48}\eta(\Delta)e^{-\gamma_1 t}\cos(2\Omega_L t), \tag{6}$$

where ϵ is the isotropic part of state. This allows one to calculate the local scaling factor as

$$\zeta(\Delta) = \frac{1}{10}\frac{\delta\alpha^{(z)}(0;\Delta)}{\delta\alpha^{(x)}(0;\Delta)}. \tag{7}$$

D. CYCLOPS-like measurements

Equation (1) shows that our reconstruction method is sensitive to the initial phase of the measured signal. As uncontrollable phase delays are present in every experiment, the identification of the quadrature components of the signal becomes difficult. To address this issue, we adapt the cyclically ordered phase sequence (CYCLOPS) method, commonly utilized in NMR [28,29]. In our approach, we leverage the fact that the π rotation of the state around the **y** axis leads to a sign reversal of $\langle\hat{\alpha}_I\rangle$ and $\langle\hat{\beta}\rangle$ (for more information, see Appendix D). At the same time, by applying the pulse rotating the state by $\pi/2$ around the **z** axis and next the pulse rotating the state around the **y** axis by π, the signs of the $\langle\hat{\alpha}_R\rangle$ and $\langle\hat{\beta}\rangle$ are reversed (see Appendix D). By subtracting these two transformed states from the initial signal, we obtain

$$(\delta\alpha - \delta\alpha^{(Y)})(t;\Delta) = 2\eta(\Delta)[-\zeta(\Delta)e^{\gamma_2 t}\langle\hat{\beta}\rangle + e^{-\gamma_1 t}\langle\hat{\alpha}_I\rangle\cos(2\Omega_L t+\varphi)], \quad (8)$$

$$(\delta\alpha - \delta\alpha^{(ZY)})(t;\Delta) = 2\eta(\Delta)[-\zeta(\Delta)e^{\gamma_2 t}\langle\hat{\beta}\rangle + e^{-\gamma_1 t}\langle\hat{\alpha}_R\rangle\sin(2\Omega_L t+\varphi)], \quad (9)$$

where φ is an unknown phase shift originating from the experimental apparatus. In our CYCLOPS-like measurements, the problem of the unknown phase is alleviated, as the final signals, given by Eqs. (9) and (10), depend only on one quadrature (via either sine or cosine time dependence) and, thus, φ becomes insignificant. The procedure also allows us to remove systematic shifts of the signals associated with the imbalance of the polarimeter (for more details, see Appendix D).

E. Technique limitations

Our technique has two main limitations. The first is associated with the intensity of the light used to probe the atoms. From the point of view of the SNR this intensity should be maximized. On the other hand, the developed theoretical model should adequately describe the considered system. The model, given in Ref. [15], assumes a negligible population of the excited state. This condition is fulfilled if the optical transition is not saturated, i.e., when

$$\kappa_o = \frac{\Omega_R^2}{\Gamma^2} \ll 1, \quad (10)$$

where κ_o is the saturation parameter of the optical transition, Ω_R is the Rabi frequency of the probe light, and Γ is the natural width of this transition. For the uncoated vapor cell, the saturation intensity of ^{87}Rb atoms which are excited at the D_1 line is 2.39 mW/cm^2. It should be noted, however, that in paraffin-coated cells the intensity saturating the optical transition needs to be normalized over the whole cell volume [30].

To fulfill the model assumptions, we also need to ensure that the probing beam is not pumping atoms, i.e., that the thermalized state (the steady state when the pump beam is switched off) differs from the isotropic state. To ensure that we can use hyperfine saturation parameter $\kappa_{\rm hf}$ [31], which also incorporates correction for the Doppler broadening of the medium and the differences between the cell volume and its illuminated part:

$$\kappa_{\rm hf} = \frac{\Omega_R^2}{\Gamma\gamma}\frac{\Gamma}{\Gamma_D}\frac{V_i}{V_c}, \quad (11)$$

where γ is the relaxation of the atomic state (in our case $\gamma = \gamma_1$), Γ_D is the Doppler width of the transition, V_i is the volume of the atoms illuminated by the probing beam, while V_c is the volume of the entire cell. Using Eq. (11) we determinate hyperfine saturation intensity as $I_{\rm sat}^{\rm hf} \approx 27.9\ \mu$W/cm^2.

Second limitation comes from the fact that it is assumed that the light characteristic parameters (amplitude, polarization angle, ellipticity, and phase) remain constant throughout the medium which holds when medium is considered to be optically thin. This allows us to approximate the initial values of the parameters during our calculations. However, in the scenarios where the medium is optically thick, we need to solve differential equations for these parameters when the light propagates through the medium [32]. As the density matrix is influenced by the light field, this leads to an increased complexity of the analysis.

IV. RECONSTRUCTION OF STATES

To perform QST, we conducted the above-described nine measurements, consisting of three sets of CYCLOPS-like pulses for each of the three control pulses. To ensure the self-consistency of our reconstruction procedure, we simultaneously fit all of the polarization-rotation signals with shared parameters, such as the global phase, relaxation rates, and oscillation frequency. The fitting values are then used to determine the observables and reconstruct the qutrit density-matrix elements using the linear inversion method given in Eq. (3). However, as this method does not guarantee the reconstructed matrices to be positive semidefinite, we utilize a maximum likelihood method with the Euclidean norm [20,33] to find the closest physical realization of the reconstructed matrix.

To validate our tomography technique, we compare the reconstructed density matrices with numerical simulations of the states obtained during the pumping stage. For the simulations, we assume the interaction of an appropriately polarized light with a Doppler-broadened medium consisting of the atoms of the energy-level structure similar to that of the D_1 line in ^{87}Rb. As in the real experiment, we assume that there are two distinct spatial regions between which the atoms can freely move. In the first region, the atoms evolve in a homogeneous magnetic field and relax to thermal equilibrium due to the collisions with vapor-cell walls and between one another. This corresponds to the atoms residing outside of the light beams. In the second region, the atoms still interact with the magnetic field, but also with the pump and repump light. Moreover, we neglect the wall relaxation in this region. The latter region corresponds to the atoms inside the light beams. All the parameters used in the simulations match the parameters of our experimental setup. We have validated the robustness of our technique by aligning experimental data with corresponding simulations of selected basic states, which we could readily generate. Looking ahead, we aim to extend this methodology to reconstruct more complex states that pose experimental challenges. This capability is crucial, especially for applications like quantum process tomography.

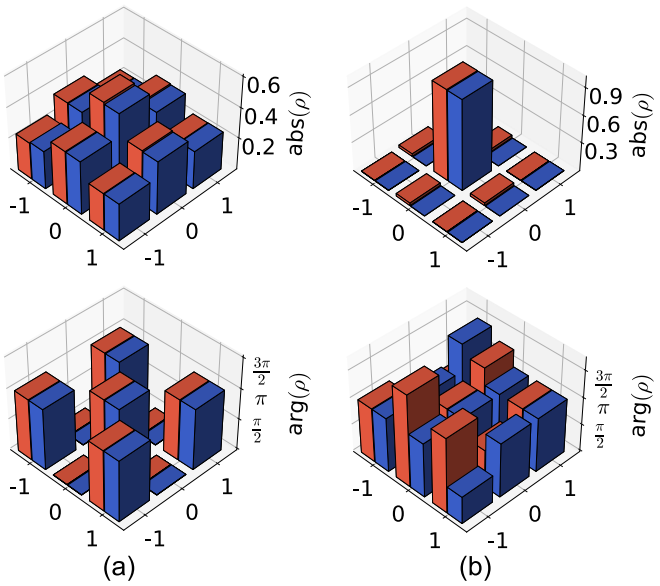

FIG. 3. Comparison of two experimentally reconstructed density matrices (blue bars), with simulated ones (red bars), including their amplitude (upper panels) and phase (lower panels). The first state (a) is pumped with circularly polarized light and the second state (b) is pumped with linearly **z**-polarized pumps, propagating along the **x** axis. The fidelity achieved between the experimental results and simulations in both cases exceeds 0.99.

As representative examples for our reconstruction, we consider two states that can be easily generated experimentally and simulated theoretically. The first state can be pumped with a strong, pumping light which is circularly polarized and propagating along the **x** axis [Fig. 3(a)]. The state has a nonuniform population distribution and all its coherences are nonzero. This allows us to demonstrate that our method can reconstruct not only different coherences, but also determine their amplitudes and phases with a high accuracy. According to the numerical simulations of the system, the repump light pumps more than 98% of the atoms into the desired hyperfine manifold and the created state is very close to the perfect pure state [fidelity of 0.96946(91)]. Main uncertainties of the pumping originate from the temporal variations in the frequency and intensity of lasers. The results of the experimental reconstruction and simulations are presented in Fig. 3(a). As can be seen, the results are in a very good agreement revealing a reconstruction fidelity of 0.995. As the second example, we considered a state pumped with the π-polarized light, propagating along the **x** axis. In the ideal case (without experimental artifacts), this scheme leads to the total depletion of the $m_F = \pm 1$ states and no coherences between any sublevels. In this case, the simulations suggest that, in our experimental conditions, over 98% of atoms are pumped into an effective pure state with a fidelity of 0.98029(38). As shown in Fig. 3(b), our measurements demonstrate a good agreement with numerical simulations, demonstrating the fidelity of 0.998. Nonetheless one can notice that a very small amplitude of the coherences can lead to the deterioration of the phase reconstruction. The very high quality of the reconstruction of these two representative states demonstrates the usefulness of our QST technique.

It is noteworthy that one of the most important advantages of this tomography technique is its significant robustness against white noise [15]. However, we also verified with numerical simulations that the robustness remains practically unchanged for the assumed noise that adequately represents experimental noise (with a specific spectral structure). Specifically, we tested the robustness of the method using the $1/f$ noise and noise arising at specific spectral components of the signal, e.g., close to the Larmor frequency, where the signal of interest arises. In the analysis, we observed a small deterioration of the methods performance, but with the SNR at a level of 5 a 0.99 fidelity was achieved.

V. CONDITIONING AND OPTIMIZATION OF QUANTUM STATE TOMOGRAPHY

A. Condition number in linear inversion

The condition number κ is a useful parameter to evaluate the reliability of a QST method [see Eq. (3)]. Specifically, to quantify the ability to tolerate errors or sensitivity to the errors, we use the condition number of a (nonsingular) matrix $\mathbb{C}$, which, assuming the spectral norm $\|\cdots\|_2$, can be defined as [34–36]

$$\begin{aligned}\kappa(\mathbb{C}) &= \|\mathbb{C}\|_2 \, \|\mathbb{C}^{-1}\|_2 \\ &= \max[\mathrm{svd}(\mathbb{C})] \max[\mathrm{svd}(\mathbb{C}^{-1})] \\ &= \frac{\max[\mathrm{svd}(\mathbb{C})]}{\min[\mathrm{svd}(\mathbb{C})]} \geqslant 1, \end{aligned} \tag{12}$$

where $\mathrm{svd}(\mathbb{C})$ denotes the singular values of $\mathbb{C}$. The significance of this error-robustness parameter explains well the Gastinel-Kahan theorem [35], which states that a relative distance of a nonsingular square matrix $\mathbb{C}$ from the set of singular matrices corresponds to the inverse of the condition number. Utilizing the error $\delta\tilde{\mathbf{b}}$ in the observation vector $\tilde{\mathbf{b}}$ and the condition number $\kappa(\mathbb{C})$, one can estimate the error $\delta\rho_V$ in the reconstructed density matrix ρ_V from the Atkinson inequalities [34]

$$\frac{1}{\kappa(\mathbb{C})} \frac{\|\delta\tilde{\mathbf{b}}\|}{\|\tilde{\mathbf{b}}\|} \leqslant \frac{\|\delta\rho_V\|}{\|\rho_V\|} \leqslant \kappa(\mathbb{C}) \frac{\|\delta\tilde{\mathbf{b}}\|}{\|\tilde{\mathbf{b}}\|}. \tag{13}$$

The above equation allows for easier and more intuitive understanding of the usefulness of the condition number. One can notice that, in the procedure of linear inversion, propagation of the experimental uncertainty highly depends on the state that is measured and which of the measured signals have higher relative uncertainties. Equation (13) allows one to make a general statement that, even though the relative uncertainty of the reconstruction is state dependent, it is also bounded by the relative uncertainty of the observation vector multiplied by $\kappa(\mathbb{C})$. This allows the interpretation that the condition number is the measure of the stability of our method or, in other words, it shows how our method in some particular cases may amplify the experimental uncertainties and errors. When the condition number approaches 1, it becomes apparent that small relative variations in the observation vector $\tilde{\mathbf{b}}$ always result in correspondingly small relative changes in the reconstructed state ρ_V. In order to account for the errors $\delta\mathbb{C}$ present in the coefficient matrix $\mathbb{C}$, these inequalities can be expanded according to the formulation derived in Ref. [34], giving rise

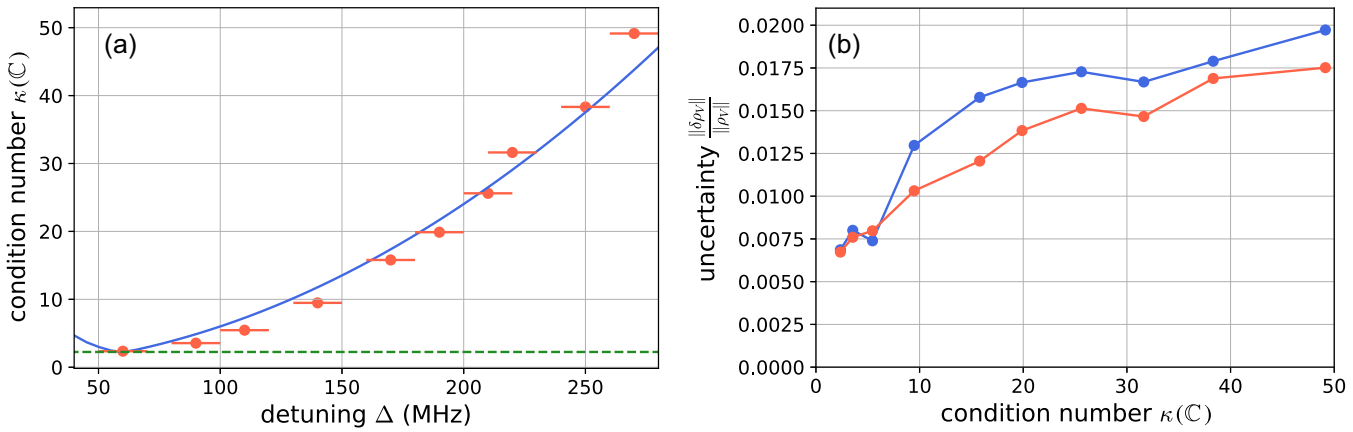

FIG. 4. (a) Condition number $\kappa(\mathbb{C})$ of a state measured versus the detuning Δ of the probing light from the center of the Doppler-broadened $f = 1 \rightarrow F = 2$ transition. The red points indicate the values calculated based on experiment (horizontal uncertainty comes from the uncertainty of detuning; the evaluated vertical errors are so small that they are not visible in the plot), while the blue curve shows the theoretical dependence calculated from the absorption measurements. The green dashed line indicates the smallest $\kappa(\mathbb{C}) = 2.25$ achievable using this approach. (b) Relative uncertainty of the linear inversion [see Eq. (13)] as a function of the condition number $\kappa(\mathbb{C})$. Red points correspond to the reconstruction of the state pumped with the circularly polarized light that propagated along the **x** axis [see Fig. 3(a)] and blue points correspond to the reconstruction of the state generated with the linearly **z**-polarized pump light, propagating along the **x** axis [see Fig. 3(b)]. It is seem that the uncertainty of the condition number is significantly smaller than the size of the data points. Solid lines are added for clarity.

to the expression

$$\frac{\|\delta\rho_V\|}{\|\rho_V\|} \leqslant \frac{\kappa(\mathbb{C})}{1-\kappa(\mathbb{C})\|\delta\mathbb{C}\|/\|\mathbb{C}\|}\left[\frac{\|\delta\tilde{\mathbf{b}}\|}{\|\tilde{\mathbf{b}}\|}+\frac{\|\delta\mathbb{C}\|}{\|\mathbb{C}\|}\right]. \quad (14)$$

By referring to the inequalities in Eqs. (13) and (14), we can infer that the quality of a QST method, in terms of its error sensitivity or robustness, can be assessed through its condition number $\kappa(\mathbb{C})$, which characterizes the degree to which small (large) changes in the observation vector $\tilde{\mathbf{b}}$ lead to relatively small (large) changes in the reconstructed state ρ_V. Thus, if $\kappa(\mathbb{C})$ is small (large), the QST method is well conditioned (ill conditioned), indicating the robustness (sensitivity) of the method to errors in the observation vector $\tilde{\mathbf{b}}$. In the case of ill-conditioned QST, even slight errors in $\tilde{\mathbf{b}}$ can cause significant errors in the reconstructed ρ_V. In short, the smaller the condition number is, the stronger robustness of a given linear-inversion-based QST method is against errors. Thus, one can refer to an optimal method in this respect if $\kappa(\mathbb{C}) = 1$. Numerical examples of ill-conditioned QST problems can be found in Refs. [17,34].

As a quantifier (or a "measure") of the "closeness" of two quantum states, which in our case correspond to the simulated state $\rho_{\text{sim}} = \rho_V$ and the experimentally reconstructed state $\rho_{\text{exp}} = \rho_V + \delta\rho_V$, one can use a mixed-state fidelity [37]. It is based on the Bures distance or the relative error (RE) in ρ_{exp}, defined as $||\rho_{\text{exp}} - \rho_{\text{sim}}||/||\rho_{\text{sim}}|| = ||\delta\rho_V||/||\rho_V||$ for a chosen norm. The estimation of the RE is especially simple by applying the Atkinson inequalities, given in Eqs. (13) and (14). Specifically, the inequalities give the lower and upper bounds on the RE in ρ_{exp} due to (i) the experimental the RE in $\tilde{\mathbf{b}}$ (both statistical and systematic), (ii) the systematic RE in $\mathbb{C}$ caused by, e.g., inaccurate experimental apparatus settings, but also (iii) the condition number κ, which is a measure of the error amplification due to the employed inversion in a given linear reconstruction procedure.

B. Optimization via probe light tuning

In order to optimize a QST process, it is desired to make the coefficient matrix $\mathbb{C}$ more isotropic, which means that each measurement brings an equal amount of information about the system. A simple example of such an optimized problem is when each measurement brings information about only a specific density-matrix element, with all measurements having the same weight [17,18]. In this case, the coefficient matrix $\mathbb{C}$ is proportional to identity. Even though such optimization is intuitive, it is often unpractical, because experimental transformations, which are required to achieve a desired scheme, are very complex. Instead, here we propose a scheme wherein a single experimental parameter is adjusted. In our case, this parameter is the probing light detuning Δ, which is incorporated in Eq. (1) through $\zeta(\Delta)$.

It is important to note that our method does not guarantee an optimal tomography process with $\kappa(\mathbb{C}) = 1$. Therefore, to explore the limit of the method, we calculate the eigenvalues of the coefficient matrix with $\zeta(\Delta)$ as a free parameter. In our case, the eigenvalues of $\mathbb{C}$ can be analytically calculated, taking the values $\{\frac{1}{100}, \frac{1}{150}, \frac{1}{225}, \frac{1}{225}, \frac{1}{225}, \frac{\zeta^2}{18}, \frac{\zeta^2}{9}, \frac{\zeta^2}{9}\}$. From this, we obtain the dependence of $\kappa(\mathbb{C})$ on $\zeta(\Delta)$ [see Fig. 4(a)] and a minimal possible conditional number, equal to 2.25 is determined.

To further illustrate the effect of the probing-light detuning on the reconstruction uncertainty and, hence, to demonstrate the potential of this approach, we perform a series of reconstructions of a state generated under the same conditions, but reconstructed using different probing-light detunings. In our experiment, the detuning is changed from 50 to 270 MHz. The results of these investigations, shown in Fig. 4(b),

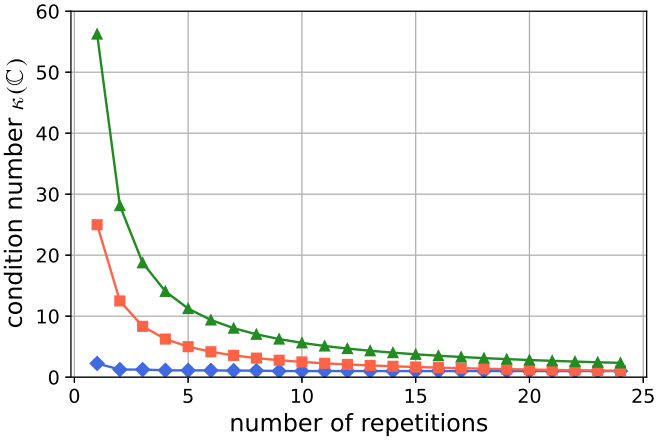

FIG. 5. Minimum achievable condition number versus a number of repetitions of specific measurements. Three sets of points correspond to the condition number at different detunings: 300 MHz (green triangles), 200 MHz (red squares), and 60 MHz (blue diamonds). The solid lines are added for eye guidance.

demonstrate that the reliability of the reconstruction deteriorates with the detuning and it achieves the minimum in the vicinity of the center of the Doppler-broadened transitions $f = 1 \rightarrow F = 2$. This agrees with our theoretical prediction of the condition-number detuning dependence, which we calculate assuming that $\zeta(\Delta) = V_I(\Delta)/V_R(\Delta)$.

C. Conditional number versus the number of measurements

The repetition of specific measurements offers a straightforward and versatile method for optimizing the relative weights of the observables used in the state-reconstruction procedure. This approach allows us to achieve the condition number arbitrarily close to 1, making it particularly valuable when the original method is infeasible or when the condition number is desired to be smaller than the detuning-optimized bound (e.g., 2.25). However, it should be noted that this technique is associated with a potential drawback. Namely the number of repetitions required to attain $\kappa(\mathbb{C}) = 1$ is typically substantial, especially when dealing with initially high condition numbers, as illustrated in Fig. 5.

VI. CONCLUSIONS

In this study, we presented an experimental implementation of the quantum-state tomography technique, which was originally proposed in Ref. [15]. The technique enabled us to successfully reconstruct collective quantum states of a qutrit in room-temperature rubidium vapor at the $f = 1$ ground state. Compared to other tomographic techniques [21,22,38,39], our method distinguishes itself with a superior fidelity, resilience against the SNR, and a straightforward control protocol. However, these advantages come at the expense of longer measurement times compared to alternative approaches. To overcome experimental challenges of the reconstruction, we adapted the CYCLOPS technique, which allowed us to achieve a reliable reconstruction by mitigating the problem of unknown phase delays present in measured signals. Additionally, we presented a comprehensive analysis of the technique by introducing the conditional number, which quantifies the reliability of the reconstruction. This parameter was investigated versus different experimental factors, including tuning of the probing light, i.e., the light used for the reconstruction. We demonstrated that, by an appropriate tuning of the light, conditional numbers as low as 2.25 can be achieved (where the conditional number of 1 refers to an ideal reconstruction). We also demonstrated that further improvement of the reconstruction (by lowering the conditional number) can be achieved by the repetition of the specific measurements.

The reported successful implementation of the presented QST technique opens up avenues for measuring a range of fundamental properties of qutrits. In the future, we plan to focus on exploring different measures of nonclassicality and establishing their ordering for various classes of quantum states. We also plan a further development of the technique to demonstrate quantum process tomography, i.e., to expand the method's capabilities in the characterization of quantum operations and transformations. Finally, the ability to accurately reconstruct the quantum states of atomic ensembles allows for an experimental optimization of the generation of metrologically appealing quantum states. This is the research direction that we currently pursue in our work.

Our findings underscore the efficacy of high-fidelity quantum-state reconstruction within room-temperature atomic vapors, showcasing the promise of this approach for advancing quantum research and applications.

ACKNOWLEDGMENTS

The authors would like to thank Arash D. Fard for his help in experimental measurements and Alexander Franzen for providing the COMPONENTLIBRARY package under the Creative Commons license, which was used to prepare the scheme of our experimental setup. The work was supported by the National Science Centre, Poland within the SONATA BIS program (Grant No. 2019/34/E/ST2/00440). M.K. would like to acknowledge support from the Excellence Initiativeof the Research University of the Jagiellonian University in Kraków. A.M. is supported by the Polish National Science Centre (NCN) under the Maestro (Grant No. DEC-2019/34/A/ST2/00081).

APPENDIX A: PRINCIPLES OF THE TOMOGRAPHY METHOD

In Ref. [15], the relation between the time- and detuning-dependent polarization rotation $\delta\alpha(t;\Delta)$ and the operators $\hat{\alpha}_{R,I}$ and $\hat{\beta}$, associated with the coherences and populations difference of specific magnetic sublevels, is given as

$$\delta\alpha(t;\Delta) = \chi e^{-\gamma t}[\langle\hat{\alpha}_R\rangle V_R(\Delta)\sin(2\Omega_L t) + \langle\hat{\alpha}_I\rangle V_R(\Delta)\cos(2\Omega_L t) - \langle\hat{\beta}\rangle V_I(\Delta)], \quad \text{(A1)}$$

where $V_R(\Delta)$ and $V_I(\Delta)$ are the real and imaginary parts of the Voigt profile, respectively, and χ is related to experimental parameters such as an atomic density and transition frequency. In order to derive Eq. (A1), the isotropic relaxation of the atomic state was assumed. This may not be the case

in a real experiment, where various experimental factors (e.g., magnetic-field gradients), may introduce additional dephasing of coherences. In turn, the off-diagonal elements of the density matrix relax faster than the diagonal ones. As the observables $\hat{\alpha}_{R,I}$ depend exclusively on the coherences, while $\hat{\beta}$ on the population imbalance, to account for the fact, we introduce two separate relaxation rates, slightly modifying Eq. (A1), i.e.,

$$\delta\alpha(t;\Delta) = \eta(\Delta)(e^{-\gamma_1 t}[\langle\hat{\alpha}_R\rangle \sin(2\Omega_L t) + \langle\hat{\alpha}_I\rangle \cos(2\Omega_L t)] - \zeta(\Delta)e^{-\gamma_2 t}\langle\hat{\beta}\rangle), \quad \text{(A2)}$$

where $\eta(\Delta) = \chi V_R(\Delta)$ and $\zeta(\Delta) = V_I(\Delta)/V_R(\Delta)$ are the global and local scaling factors, respectively.

The expectation values $\langle\hat{\alpha}_{R,I}\rangle$ and $\langle\hat{\beta}\rangle$ depend on the population deference and the coherences between the states of the magnetic quantum-number difference $\Delta m_F = 2$. Thus, the operators do not allow one to reconstruct an entire density matrix of the system. In order to access the remaining density-matrix elements (e.g., the coherences with the $\Delta m_F = 1$), one needs to transform the measured observables, so that the overall set of measurements defines a positive operator-valued measure (POVM) [21]. This can be achieved by introducing the unitary-evolution operators U_i, commonly called the control pulses, which modify the observable $\hat{O}$ in the following manner:

$$\mathrm{Tr}\,[\hat{O}U_i\rho U_i^\dagger] = \langle U_i^\dagger \hat{O} U_i\rangle = \langle\hat{O}'\rangle, \quad \text{(A3)}$$

where $\hat{O}$ can be either $\hat{\alpha}_{R,I}$ or $\hat{\beta}$. With the set of the observables $\hat{O}_i$, one can present the reconstruction problem in vectorized forms as given by Eqs. (2) and (3).

It should be noted that reconstruction based on Eq. (3) may produce unphysical results, which arise when the reconstructed density matrix is not positive semidefinite. In such a case, one may use several techniques to find a corresponding physical realization of the matrix. The simplest approach is to set negative eigenvalues to zero and renormalize the density matrix. More elaborate techniques find the closest positive semidefinite matrix using different norms using, for example, a maximum likelihood method [20,33]. In the presented work, we use such a method, assuming that a distance between matrices is based on the Euclidean norm,

$$d^2(\mathbb{A},\mathbb{B}) = \sum_{ij} |\mathbb{A} - \mathbb{B}|_{ij}^2. \quad \text{(A4)}$$

The applied implementation of the method allows us to obtain a physical density matrix, which gives the best approximation of the measured observables.

APPENDIX B: RECONSTRUCTION OF QUTRIT STATES

The general theoretical discussion presented in this paper may be used to reconstruct a three-level system (qutrit). In our work, such a system is implemented using the ground-state hyperfine level of ^{87}Rb of the total angular momentum $f = 1$ (Fig. 1). In this case, the density matrix can be written as

$$\rho = \begin{bmatrix} \rho_{\bar{1}\bar{1}}^R & \rho_{\bar{1}0}^R + i\rho_{\bar{1}0}^I & \rho_{\bar{1}1}^R + i\rho_{\bar{1}1}^I \\ \rho_{\bar{1}0}^R - i\rho_{\bar{1}0}^I & 1 - \rho_{\bar{1}\bar{1}}^R - \rho_{11}^R & \rho_{01}^R + i\rho_{01}^I \\ \rho_{\bar{1}1}^R - i\rho_{\bar{1}1}^I & \rho_{01}^R - i\rho_{01}^I & \rho_{11}^R \end{bmatrix}, \quad \text{(B1)}$$

where $\bar{1} = -1$. It follows from above that $\mathrm{Tr}(\rho) = 1$. It is noteworthy that the normalization of the density matrix modifies the vector **b** by shifting its elements by a fixed value. It can be shown [15] that, for a system probed on the transition $f = 1 \to F = 2$ (Fig. 1), the observables $\hat{\alpha}_{R,I}$ and $\hat{\beta}$ are given by

$$\hat{\alpha}_R = \frac{\hat{d}_+^2 + \hat{d}_-^2}{||\hat{d}||} = \frac{1}{30}(|\bar{1}\rangle\langle 1| + |1\rangle\langle\bar{1}|), \quad \text{(B2a)}$$

$$\hat{\alpha}_I = \frac{i(\hat{d}_+^2 - \hat{d}_-^2)}{||\hat{d}||} = \frac{i}{30}(|\bar{1}\rangle\langle 1| - |1\rangle\langle\bar{1}|), \quad \text{(B2b)}$$

$$\hat{\beta} = \frac{\hat{d}_+\hat{d}_- - \hat{d}_-\hat{d}_+}{||\hat{d}||} = \frac{1}{6}(|\bar{1}\rangle\langle\bar{1}| - |1\rangle\langle 1|), \quad \text{(B2c)}$$

where $\hat{d}_\pm$ are the dipole operators associated with the right (+) and left (−) circular polarization components of the linearly polarized probe light, and $\|\hat{d}\|$ is the reduced dipole-matrix element corresponding to the transition.

To expand the set of observables used for tomography, we introduce the control pulses U_i implemented as pulses of a DC or nonoscillating magnetic field that induce a geometrical rotation of the spin polarization by $\pi/2$ around the **x** or **y** axes. The explicit forms of the control pulses are

$$U_x = \frac{1}{2}\begin{bmatrix} 1 & i\sqrt{2} & -1 \\ i\sqrt{2} & 0 & i\sqrt{2} \\ -1 & i\sqrt{2} & 1 \end{bmatrix}, \quad \text{(B3a)}$$

$$U_y = \frac{1}{2}\begin{bmatrix} 1 & -\sqrt{2} & 1 \\ \sqrt{2} & 0 & -\sqrt{2} \\ 1 & \sqrt{2} & 1 \end{bmatrix}. \quad \text{(B3b)}$$

Applying U_x and U_y to the operators given by Eqs. (B2) allows one to relate the observables $\alpha_{R,I}$ and β with all the other density-matrix elements and, hence, reconstruct the whole density matrix.

APPENDIX C: DERIVATION OF SCALING FACTORS

1. Global scaling factor

An essential parameter of the presented QST technique is the global scaling factor $\eta(\Delta)$ in Eq. (A2). The most convenient way to calculate this parameter is based on the measurements of the absorption of light by completely unpolarized atoms. From the formula describing the change in the amplitude of the light traversing a medium, given in Ref. [15], one obtains

$$\frac{\delta E}{E}(t;\Delta) = \frac{2\eta(\Delta)}{2f+1}\sum_{n=-f}^{f}\begin{pmatrix} f & 1 & F \\ -n & 1 & n-1 \end{pmatrix}^2, \quad \text{(C1)}$$

where f and F are the total angular momenta of the ground and excited states, respectively, which for our system are $f = 1$ and $F = 2$. Additionally, one should notice that this model was derived for a two-level system, while in more complex systems of ^{87}Rb, where the two ground states $f = 1$ and $f = 2$ exist, the absorption of light tuned to the $f = 1$ ground state results only from 3/8 of the total number of atoms in the sample. As in our experimental procedure, we

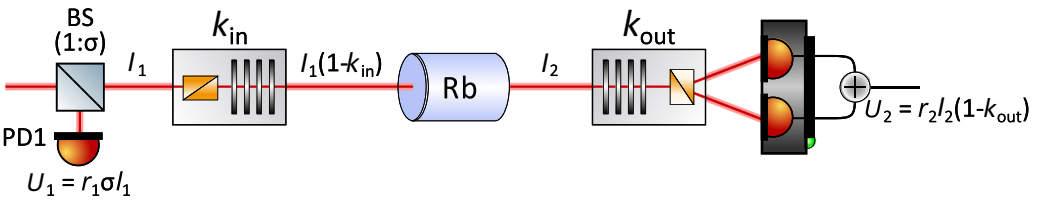

FIG. 6. Simplified scheme of the experimental setup used for the measurements of the global scaling factor $\eta(\Delta)$. A nonpolarizing beam splitter (BS) with 1-to-σ splitting ratio is used to measure the light intensity before the it enters atomic ensemble. The light intensity is measured as a voltage $U_1(\Delta) = r_1\sigma I_1(\Delta)$, where r_1 is the light power-voltage conversion factor in a transimpedance photodetector detector (PD1). The light intensity is written as a function of the light detuning Δ to highlight the fact that the changes in the light frequency usually introduce the corresponding changes in the light intensity emitted by the laser. After BS, there are various optical elements, introducing intensity losses k_{in}, and a vapor cell containing atoms whose state is to be reconstructed. Next, the beam experiences losses, k_{out}, due to the elements situated after the cell, and finally the light is split using the balanced polarimeter, consisting of a Wollastone prism and a balanced photodetector. The output signal U_2 is the sum of the voltages measured by each of the PDs that constitute the balanced photodetector. Both PDs have the same conversion gain r_2, thus $U_2(\Delta) = r_2 I_2(\Delta)(1 - k_{\text{out}})$.

repump all the atoms in the $f = 1$ state, and then Eq. (C1) needs to be modified to account for the fact:

$$\frac{\delta E}{E}(t;\Delta) = \frac{8}{3}\frac{2\eta(\Delta)}{3}\sum_{n=-1}^{1}\begin{pmatrix}1 & 1 & 2\\ -n & 1 & n-1\end{pmatrix}^2 = \frac{16}{27}\eta(\Delta). \tag{C2}$$

Since the amplitude of light is not a parameter easily measurable experimentally, it is more convenient to replace the light-amplitude change by the light-intensity change,

$$\frac{\delta E}{E} = \sqrt{1+\frac{\delta I}{I}} - 1, \tag{C3}$$

where I is the probing light intensity and δI is the change of the light intensity resulting from the absorption in the medium (note that δI is negative).

In a real experiment, the intensity of transmitted light can be influenced by losses at different optical elements within the system (e.g., glass walls of the vapor cell). For a reliable reconstruction, it is crucial to distinguish these losses from the light absorption in the medium. To address this problem, we measure the sum of the two outputs of a balanced polarimeter used for the state reconstruction and the intensity of light before its transmission through the atomic ensemble (Fig. 6). This allows us to write

$$\frac{\delta I}{I} = \frac{I_2(\Delta) - I_1(\Delta)(1-k_{\text{in}})}{I_1(\Delta)(1-k_{\text{in}})} = \frac{r_1\sigma}{r_2(1-k_{\text{in}})(1-k_{\text{out}})}\frac{U_2(\Delta)}{U_1(\Delta)} - 1. \tag{C4}$$

The most convenient way to determine the overall scaling [corresponding to the first term in Eq. (C4)] is to measure the signal for a far-detuned light, $\Delta \to \infty$. As in this case, the light absorption is negligibly small, and one obtains

$$\frac{U_1(\infty)}{U_2(\infty)} = \frac{r_1\sigma}{r_2(1-k_{\text{in}})(1-k_{\text{out}})}. \tag{C5}$$

Combining Eqs. (C2)–(C5), we obtain the final relation for the global scaling factor $\eta(\Delta)$, which is given by

$$\eta(\Delta) = \frac{27}{16}\left(\sqrt{\frac{U_1(\infty)}{U_2(\infty)}\frac{U_2(\Delta)}{U_1(\Delta)}} - 1\right). \tag{C6}$$

2. Local scaling factor

The second important parameter that is needed for the tomography method is the local scaling factor $\zeta(\Delta)$. As discussed in the main text, to calculate the parameter we compare the rotation signals measured for the "stretched" states pumped along the **x** and **z** axes, which are given by the density matrices

$$\rho_z = (1-\epsilon)\begin{bmatrix}0&0&0\\0&0&0\\0&0&1\end{bmatrix} + \frac{\epsilon}{3}\mathbb{1}, \tag{C7a}$$

$$\rho_x = (1-\epsilon)\begin{bmatrix}\frac{1}{4}&-\frac{1}{2\sqrt{2}}&\frac{1}{4}\\-\frac{1}{2\sqrt{2}}&\frac{1}{2}&-\frac{1}{2\sqrt{2}}\\\frac{1}{4}&-\frac{1}{2\sqrt{2}}&\frac{1}{4}\end{bmatrix} + \frac{\epsilon}{3}\mathbb{1}. \tag{C7b}$$

Here, we assumed a small imperfection in pumping manifesting through the isotropic term of the amplitude ϵ. It is noteworthy that none of the observables used for the state reconstruction [given by Eqs. (B2)] generates any signal corresponding to the isotropic term ($\epsilon = 0$). Using Eqs. (B2) and (A2) allows one to calculate the corresponding rotation signals for the two cases,

$$\delta\alpha^{(z)}(t;\Delta) = -\frac{5(1-\epsilon)}{24}\eta(\Delta)\zeta(\Delta)e^{-\gamma_2 t}, \tag{C8a}$$

$$\delta\alpha^{(x)}(t;\Delta) = -\frac{(1-\epsilon)}{48}\eta(\Delta)e^{-\gamma_1 t}\cos(2\Omega_L t). \tag{C8b}$$

By including the amplitudes of the oscillatory and DC parts of the signals, the local scaling factor can be finally calculated as

$$\zeta(\Delta) = \frac{1}{10}\frac{\delta\alpha^{(z)}(0;\Delta)}{\delta\alpha^{(x)}(0;\Delta)}. \tag{C9}$$

APPENDIX D: CYCLOPS-LIKE MEASUREMENTS

In a real experiment, an oscillating part of the polarization-rotation signal may experience additional phase shift φ and the whole signal may have a DC offset, D. Thus, Eq. (A2) is modified to

$$\begin{aligned}\delta\alpha(t;\Delta) = \eta(\Delta)\big([\langle\hat{\alpha}_R\rangle \sin(2\Omega_L t+\varphi) \\ + \langle\hat{\alpha}_I\rangle \cos(2\Omega_L t+\varphi)]e^{-\gamma_1 t} \\ - \zeta(\Delta)\langle\hat{\beta}\rangle e^{-\gamma_2 t}\big) + D. \end{aligned} \tag{D1}$$

These additional factors may arise due to electronics or the imbalance of the polarimeter. As the reconstruction method requires fine determination of the quadrature components of the signal, one concludes that knowing the precise value of φ is needed. In our work, we use a slightly different approach, incorporating a π rotation around the **y** axis, i.e.,

$$U_y(\alpha) = \begin{bmatrix} \cos^2\left(\frac{\alpha}{2}\right) & -\frac{\sin(\alpha)}{\sqrt{2}} & \sin^2\left(\frac{\alpha}{2}\right) \\ \frac{\sin(\alpha)}{\sqrt{2}} & \cos(\alpha) & -\frac{\sin(\alpha)}{\sqrt{2}} \\ \sin^2\left(\frac{\alpha}{2}\right) & \frac{\sin(\alpha)}{\sqrt{2}} & \cos^2\left(\frac{\alpha}{2}\right) \end{bmatrix},$$

$$U_y(\pi) = \begin{bmatrix} 0 & 0 & 1 \\ 0 & -1 & 0 \\ 1 & 0 & 0 \end{bmatrix}. \tag{D2}$$

This results in a sign change in $\langle\hat{\alpha}_I\rangle$ and $\langle\hat{\beta}\rangle$,

$$\left\langle\hat{\alpha}_R^{(Y)}\right\rangle = \langle U_y(\pi)^\dagger \hat{\alpha}_R U_y(\pi)\rangle = \langle\hat{\alpha}_R\rangle, \tag{D3a}$$

$$\left\langle\hat{\alpha}_I^{(Y)}\right\rangle = \langle U_y(\pi)^\dagger \hat{\alpha}_I U_y(\pi)\rangle = -\langle\hat{\alpha}_I\rangle, \tag{D3b}$$

$$\langle\hat{\beta}^{(Y)}\rangle = \langle U_y(\pi)^\dagger \hat{\beta} U_y(\pi)\rangle = -\langle\hat{\beta}\rangle. \tag{D3c}$$

For such a pulse, the rotation signal is given by

$$\begin{aligned}\delta\alpha(t;\Delta) = \eta(\Delta)([\langle\hat{\alpha}_R\rangle \sin(2\Omega_L t+\varphi) \\ - \langle\hat{\alpha}_I\rangle \cos(2\Omega_L t+\varphi)]e^{-\gamma_1 t} \\ + \zeta(\Delta)\langle\hat{\beta}\rangle e^{-\gamma_2 t}) + D. \end{aligned} \tag{D4}$$

Calculating the difference between the signal with and without the pulse, one obtains

$$\begin{aligned}(\delta\alpha - \delta\alpha^{(Y)})(t;\Delta) = 2\eta(\Delta)[-\zeta(\Delta)e^{\gamma_2 t}\langle\hat{\beta}\rangle \\ + e^{-\gamma_1 t}\langle\hat{\alpha}_I\rangle \cos(2\Omega_L t+\varphi)]. \end{aligned} \tag{D5}$$

As can be seen, this difference depends only on a single oscillatory component, thus there is no problem with determining the initial phase. Additionally, one can see that the difference is free from the offset due to the imbalance of the polarimeter.

In a similar fashion, one can obtain a signal containing the second quadrature using the following sequence of two pulses, with the first pulse introducing the rotation around the **y** axis by π (being identical to the previous pulse), and the second pulse generating the rotation by $\pi/2$ around the **z** axis:

$$U_z(\alpha) = \begin{bmatrix} e^{-i\alpha} & 0 & 0 \\ 0 & 1 & 0 \\ 0 & 0 & e^{i\alpha} \end{bmatrix},$$

$$U_{zy} = U_z(\pi/2)U_y(\pi) = \begin{bmatrix} 0 & 0 & -i \\ 0 & -1 & 0 \\ i & 0 & 0 \end{bmatrix}. \tag{D6}$$

The pulses transform the expectation values of the observables as

$$\langle\hat{\alpha}_R^{(ZY)}\rangle = \langle U_{zy}^\dagger \hat{\alpha}_R U_{zy}\rangle = -\langle\hat{\alpha}_R\rangle, \tag{D7a}$$

$$\left\langle\hat{\alpha}_I^{(ZY)}\right\rangle = \langle U_{zy}^\dagger \hat{\alpha}_I U_{zy}\rangle = \langle\hat{\alpha}_I\rangle, \tag{D7b}$$

$$\langle\hat{\beta}^{(ZY)}\rangle = \langle U_{zy}^\dagger \hat{\beta} U_{zy}\rangle = -\langle\hat{\beta}\rangle, \tag{D7c}$$

which allows one to calculate the rotation difference,

$$\begin{aligned}(\delta\alpha - \delta\alpha^{(ZY)})(t;\Delta) = 2\eta(\Delta)[-\zeta(\Delta)e^{\gamma_2 t}\langle\hat{\beta}\rangle \\ + e^{-\gamma_1 t}\langle\hat{\alpha}_R\rangle \sin(2\Omega_L t+\varphi)]. \end{aligned} \tag{D8}$$

Similarly to the former case, the signal contains the information about only one quadrature and no dependence on the polarimeter imbalance.

The robustness of the signal against the unknown phase shift or the signal offset motivated us to use the CYCLOPS pulses for our quantum-state reconstruction.

APPENDIX E: EXAMPLES OF RECONSTRUCTION

In order to illustrate the reconstruction of a qutrit state, we utilize six experimental polarization rotations, presented in Fig. 7. The signals were observed for the state generated with the circularly polarized light, propagating along the **x** axis.

The reconstruction process involved several stages. First, we measured the absorption of the probing light in an unpolarized sample to determine the global scaling factor (see Sec. III C). In the considered experiment, we obtained $\eta(\Delta) = 0.3236(21)$. To determine the local scaling factor, we pumped our ensemble using a circularly polarized light propagating along the **x** axis to prepare a stretched state in this direction [see Sec. III C and Fig. 8(a)]. We compare the signal with the similar results obtained with and without a magnetic $\pi/2$ pulse applied along the **y** direction [see Fig. 8(b)]. This allowed us to determine the local scaling factor, which, in the considered case, was $\zeta(\Delta) = -0.4790(12)$. Next, we recorded nine signals measured with the control pulses. For each control-pulse sequence (no pulse, $\pi/2$ rotation around the **y** axis, and $\pi/2$ rotation around the **x** axis), we employed three different sets of the CYCLOPS pulses (no CYCLOPS pulse, a pulse in the **y** direction, and a CYCLOPS pulse in the **z** and then **y** directions). These signals are used to generate the difference signals [Eqs. (D5) and (D8)], which are shown in Fig. 7, and then are fitted to reconstruct the expectation values of the required operators. This is done with shared parameters, including the frequency, global phase, and relaxation rates. Finally, we used nine reconstructed observables to perform linear inversion [according to Eq. (3)], and, thus to obtain a matrix corresponding to the state. In the considered case, we

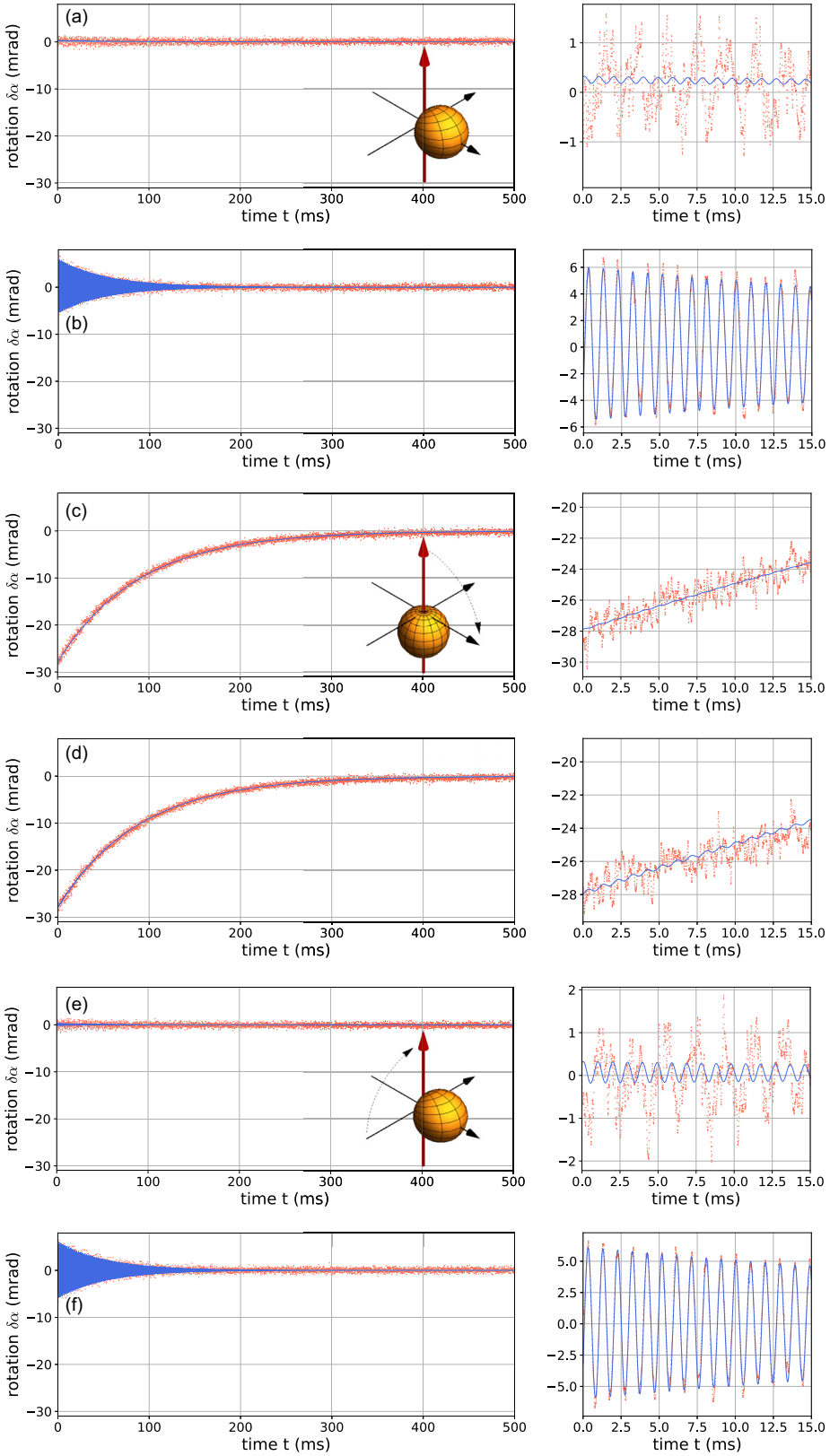

FIG. 7. Detected polarization rotations (red dots) and fitted dependences (blue lines), corresponding to the first [Eq. (D5)] (a) and the second [Eq. (D8)] (b) quadratures of the signal measured without the control pulses. (c) and (d) correspond to the same signals measured with the pulse rotating the state by $\pi/2$ around the **y** axis, while (e) and (f) correspond to the pulse rotating the state by $\pi/2$ around the **x** axis. The right column shows magnifications of the first 15 ms of the registered signals. The insets in (a), (c), and (e) show the angular-momentum probability surfaces [40] of the reconstructed state after respective rotations (denoted with black dashed arrows). The red axis denotes the axis of the magnetic field applied during detection, which coincides with the probe-light propagation direction.

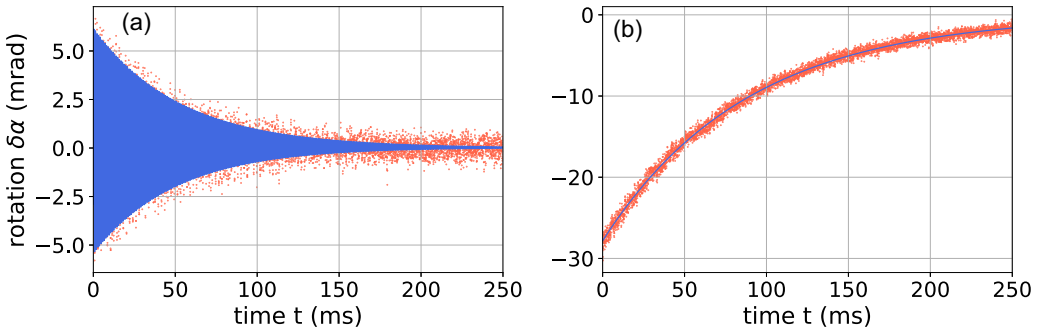

FIG. 8. Results of the measurement of the atomic response when the atoms are polarized along (a) **x** and (b) **z** axes. Based on the measurements, the local scaling factor was determined as $\zeta(\Delta) = -0.4790(12)$.

obtained

$$\rho = \begin{bmatrix} 0.2363 & -0.3903 - 0.0002i & 0.2748 - 0.0033i \\ -0.3903 + 0.0002i & 0.5175 & -0.3737 + 0.0022i \\ 0.2748 + 0.0033i & -0.3737 - 0.0022i & 0.2461 \end{bmatrix}. \tag{E1}$$

It is evident from its eigenvalues, $\mathrm{eig}(\rho) = \{1.057, -0.041, -0.016\}$, that the reconstructed matrix is not positive semidefinite. In order to address this problem, at the last stage, we applied the maximum likelihood method [33] to find the positive semidefinite matrix closest to the reconstructed one. This process allowed us to obtain the following density matrix:

$$\rho_{ML} = \begin{bmatrix} 0.2410 & -0.3507 + 0.0003i & 0.2447 - 0.0020i \\ -0.3507 - 0.0003i & 0.5104 & -0.3562 + 0.0027i \\ 0.2447 + 0.0020i & -0.3562 - 0.0027i & 0.2486 \end{bmatrix}, \tag{E2}$$

with nonegative eigenvalues, $\mathrm{eig}(\rho) = \{1, 0, 0\}$. This state is graphically presented in Fig. 3(a).

[1] K. Mouloudakis, G. Vasilakis, V. G. Lucivero, J. Kong, I. K. Kominis, and M. W. Mitchell, Effects of spin-exchange collisions on the fluctuation spectra of hot alkali-metal vapors, Phys. Rev. A **106**, 023112 (2022).

[2] R. Shaham, O. Katz, and O. Firstenberg, Strong coupling of alkali-metal spins to noble-gas spins with an hour-long coherence time, Nat. Phys. **18**, 506 (2022).

[3] W. Happer, Optical pumping, Rev. Mod. Phys. **44**, 169 (1972).

[4] O. Schmidt, R. Wynands, Z. Hussein, and D. Meschede, Steep dispersion and group velocity below c/3000 in coherent population trapping, Phys. Rev. A **53**, R27(R) (1996).

[5] K. Hammerer, K. Mølmer, E. S. Polzik, and J. I. Cirac, Light-matter quantum interface, Phys. Rev. A **70**, 044304 (2004).

[6] H. Krauter, C. A. Muschik, K. Jensen, W. Wasilewski, J. M. Petersen, J. I. Cirac, and E. S. Polzik, Entanglement generated by dissipation and steady state entanglement of two macroscopic objects, Phys. Rev. Lett. **107**, 080503 (2011).

[7] O. Katz, R. Shaham, E. S. Polzik, and O. Firstenberg, Long-lived entanglement generation of nuclear spins using coherent light, Phys. Rev. Lett. **124**, 043602 (2020).

[8] K. Jensen, W. Wasilewski, H. Krauter, T. Fernholz, B. M. Nielsen, M. Owari, M. B. Plenio, A. Serafini, M. M. Wolf, and E. S. Polzik, Quantum memory for entangled continuous-variable states, Nat. Phys. **7**, 13 (2011).

[9] M. Dąbrowski, M. Parniak, and W. Wasilewski, Einstein–Podolsky–Rosen paradox in a hybrid bipartite system, Optica **4**, 272 (2017).

[10] E. E. Mikhailov and I. Novikova, Low-frequency vacuum squeezing via polarization self-rotation in Rb vapor, Opt. Lett. **33**, 1213 (2008).

[11] I. H. Agha, G. Messin, and P. Grangier, Generation of pulsed and continuous-wave squeezed light with ^{87}Rb vapor, Opt. Express **18**, 4198 (2010).

[12] W. Wasilewski, T. Fernholz, K. Jensen, L. S. Madsen, H. Krauter, C. Muschik, and E. S. Polzik, Generation of two-mode squeezed and entangled light in a single temporal and spatial mode, Opt. Express **17**, 14444 (2009).

[13] A. Heifetz, A. Agarwal, G. C. Cardoso, V. Gopal, P. Kumar, and M. S. Shahriar, Super efficient absorption filter for quantum memory using atomic ensembles in a vapor, Opt. Commun. **232**, 289 (2004).

[14] M. Dąbrowski, R. Chrapkiewicz, and W. Wasilewski, Magnetically tuned, robust and efficient filtering system for spatially multimode quantum memory in warm atomic vapors, J. Mod. Opt. **63**, 2029 (2016).

[15] M. Kopciuch and S. Pustelny, Optical reconstruction of the collective density matrix of a qutrit, Phys. Rev. A **106**, 022406 (2022).

[16] Y. I. Bogdanov, G. Brida, M. Genovese, S. P. Kulik, E. V. Moreva, and A. P. Shurupov, Statistical estimation of the efficiency of quantum state tomography protocols, Phys. Rev. Lett. **105**, 010404 (2010).

[17] A. Miranowicz, K. Bartkiewicz, J. Peřina, M. Koashi, N. Imoto, and F. Nori, Optimal two-qubit tomography based on local

and global measurements: Maximal robustness against errors as described by condition numbers, Phys. Rev. A **90**, 062123 (2014).

[18] K. Bartkiewicz, A. Černoch, K. Lemr, and A. Miranowicz, Priority choice experimental two-qubit tomography: Measuring one by one all elements of density matrices, Sci. Rep. **6**, 19610 (2016).

[19] S. S. Roy and T. S. Mahesh, Density matrix tomography of singlet states, J. Magn. Reson. **206**, 127 (2010).

[20] A. Miranowicz, S. K. Özdemir, J. Bajer, G. Yusa, N. Imoto, Y. Hirayama, and F. Nori, Quantum state tomography of large nuclear spins in a semiconductor quantum well: Optimal robustness against errors as quantified by condition numbers, Phys. Rev. B **92**, 075312 (2015).

[21] I. H. Deutsch and P. S. Jessen, Quantum control and measurement of atomic spins in polarization spectroscopy, Opt. Commun. **283**, 681 (2010).

[22] C. Lovecchio, S. Cherukattil, B. Cilenti, I. Herrera, F. S. Cataliotti, S. Montangero, T. Calarco, and F. Caruso, Quantum state reconstruction on atom-chips, New J. Phys. **17**, 093024 (2015).

[23] K. Hammerer, A. S. Sørensen, and E. S. Polzik, Quantum interface between light and atomic ensembles, Rev. Mod. Phys. **82**, 1041 (2010).

[24] Y. Takahashi, K. Honda, N. Tanaka, K. Toyoda, K. Ishikawa, and T. Yabuzaki, Quantum nondemolition measurement of spin via the paramagnetic Faraday rotation, Phys. Rev. A **60**, 4974 (1999).

[25] G. Colangelo, R. J. Sewell, N. Behbood, F. M. Ciurana, G. Triginer, and M. W. Mitchell, Quantum atom–light interfaces in the Gaussian description for spin-1 systems, New J. Phys. **15**, 103007 (2013).

[26] D. D'Alessandro, *Introduction to Quantum Control and Dynamics* (CRC, Boca Raton, FL, 2021).

[27] S. Pustelny, V. Schultze, T. Scholtes, and D. Budker, Dichroic atomic vapor laser lock with multi-gigahertz stabilization range, Rev. Sci. Instrum. **87**, 063107 (2016).

[28] R. Freeman, *A Handbook of Nuclear Magnetic Resonance* (Longman Scientific & Technical, London, 1987).

[29] F. A. Bonk, E. R. deAzevedo, R. S. Sarthour, J. D. Bulnes, J. C. C. Freitas, A. P. Guimarães, I. S. Oliveira, and T. J. Bonagamba, Quantum logical operations for spin 3/2 quadrupolar nuclei monitored by quantum state tomography, J. Magn. Reson. **175**, 226 (2005).

[30] E. Zhivun, A. Wickenbrock, J. Sudyka, B. Patton, S. Pustelny, and D. Budker, Vector light shift averaging in paraffin-coated alkali vapor cells, Opt. Express **24**, 15383 (2016).

[31] M. Auzinsh, D. Budker, and S. M. Rochester, Light-induced polarization effects in atoms with partially resolved hyperfine structure and applications to absorption, fluorescence, and nonlinear magneto-optical rotation, Phys. Rev. A **80**, 053406 (2009).

[32] M. Auzinsh, D. Budker, and S. M. Rochester, *Optically Polarized Atoms: Understanding Light-Atom Interactions* (Oxford University Press, Oxford, 2010).

[33] M. Paris and J. Řehaček, *Quantum State Estimation*, Lecture Notes in Physics Vol. 649 (Springer, Berlin, 2004).

[34] K. E. Atkinson, *An Introduction to Numerical Analysis* (Wiley, New York, 1989).

[35] N. J. Higham, *Accuracy and Stability of Numerical Algorithms* (SIAM, Philadelphia, 1996).

[36] G. H. Golub and C. F. Van Loan, *Matrix Computations* (Johns Hopkins University Press, Baltimore 1996).

[37] P. Zanardi, H. T. Quan, X. Wang, and C. P. Sun, Mixed-state fidelity and quantum criticality at finite temperature, Phys. Rev. A **75**, 032109 (2007).

[38] T. Fernholz, H. Krauter, K. Jensen, J. F. Sherson, A. S. Sørensen, and E. S. Polzik, Spin squeezing of atomic ensembles via nuclear-electronic spin entanglement, Phys. Rev. Lett. **101**, 073601 (2008).

[39] G. M. D'Ariano, L. Maccone, and M. Paini, Spin tomography, J. Opt. B: Quantum Semiclass. Opt. **5**, 77 (2003).

[40] S. M. Rochester and D. Budker, Atomic polarization visualized, Am. J. Phys. **69**, 450 (2001).